Article

Thermal Patterns at the Campi Flegrei Caldera Inferred from Satellite Data and Independent Component Analysis

Francesco Mercogliano [1,2,3], **Andrea Barone** [2,3,*], **Luca D'Auria** [4], **Raffaele Castaldo** [2,3], **Malvina Silvestri** [5], **Eliana Bellucci Sessa** [6], **Teresa Caputo** [6], **Daniela Stroppiana** [7], **Stefano Caliro** [6], **Carmine Minopoli** [6], **Rosario Avino** [6] and **Pietro Tizzani** [2,3]

1 Dipartimento di Ingegneria (DI), Università degli Studi di Napoli 'Parthenope', Centro Direzionale Isola C4, 80143 Naples, Italy; francesco.mercogliano001@studenti.uniparthenope.it
2 Istituto per il Rilevamento Elettromagnetico dell'Ambiente, Consiglio Nazionale delle Ricerche (IREA CNR), Via Diocleziano, 328, 80124 Naples, Italy; castaldo.r@irea.cnr.it (R.C.); tizzani.p@irea.cnr.it (P.T.)
3 GAIA iLAB at the CNR—Portici Research Center, Piazzale E. Fermi 1, 80055 Portici, Italy
4 Instituto Volcanológico de Canarias (INVOLCAN), Calle Irlanda 2, 38400 Puerto de La Cruz, Tenerife, Spain; ldauria@iter.es
5 Istituto Nazionale di Geofisica e Vulcanologia (INGV), Osservatorio Nazionale Terremoti, Via di Vigna Murata, 605, 00143 Rome, Italy; malvina.silvestri@ingv.it
6 Istituto Nazionale di Geofisica e Vulcanologia (INGV), Sezione di Napoli Osservatorio Vesuviano, Via Diocleziano, 328, 80124 Naples, Italy; eliana.bellucci@ingv.it (E.B.S.); teresa.caputo@ingv.it (T.C.); stefano.caliro@ingv.it (S.C.); carmine.minopoli@ingv.it (C.M.); rosario.avino@ingv.it (R.A.)
7 Istituto per il Rilevamento Elettromagnetico dell'Ambiente, Consiglio Nazionale delle Ricerche (IREA CNR), Via A. Corti, 12, 20133 Milan, Italy; stroppiana.d@irea.cnr.it
* Correspondence: barone.a@irea.cnr.it

Abstract: In volcanic regions, the analysis of Thermal InfraRed (TIR) satellite imagery for Land Surface Temperature (LST) retrieval is a valid technique to detect ground thermal anomalies. This allows us to achieve rapid characterization of the shallow thermal field, supporting ground surveillance networks in monitoring volcanic activity. However, surface temperature can be influenced by processes of different natures, which interact and mutually interfere, making it challenging to interpret the spatio-temporal variations in the LST parameter. In this paper, we use a workflow to detect the main thermal patterns in active volcanic areas by analyzing the Independent Component Analysis (ICA) results applied to satellite nighttime TIR imagery time series. We employed the proposed approach to study the surface temperature distribution at the Campi Flegrei caldera volcanic site (Southern Italy, Naples) during the 2013–2022 time interval. The results revealed the contribution of four main distinctive thermal patterns, which reflect the endogenous processes occurring at the Solfatara crater, the environmental processes affecting the Agnano plain, the unique microclimate of the Astroni crater, and the morphoclimatic aspects of the entire volcanic area.

1. Introduction

Over the last few decades, satellite Remote Sensing in the Thermal InfraRed (TIR; 3–14 µm) domain has been widely used for different purposes since satellite sensors constantly acquire images of the Earth's surface in different TIR bands [1–5]. The availability of free and open access historical catalogues easily allows for the analysis of the surface's thermal properties and their variation over space and time by evaluating parameters, such as the Land Surface Temperature (LST), which effectively represents the measure of the surface radiative skin temperature [6–9]. According to the satellite mission features, the LST parameter can be retrieved starting from images with different spatial and temporal resolutions [10]. For example, high temporal and low spatial resolutions (i.e., >1 km and

<15 min) characterize satellites such as the Meteosat constellation and the Geostationary Environmental Satellites (GOES) [11–13], while moderate temporal and spatial resolutions (i.e., <1 km and ≈1 day) are related to satellite sensors like the Advanced Very High-Resolution Radiometer (AVHRR), the Moderate Resolution Imaging Spectroradiometer (MODIS), and Sea and Land Surface Temperature Radiometer (SLSTR) [14,15]; sensors and missions such as the Advanced Spaceborne Thermal Emission Radiometer (ASTER) and Landsat-8 can instead provide information with a spatial resolution of 100 m and a temporal one of 16 days [16]. Moreover, depending on the acquired bands, the LST parameter can be inferred by applying different methodologies, such as the Single-Channel Algorithm (SCA) and the Mono-Window Algorithm (MWA), which involve one TIR band, or the Multi-Channel algorithm (MCA) that is based on the use of more than one TIR band [17–19]. The employment of a different methodology can also affect the accuracy and the resolution of LST estimation [20].

In volcanic and hydrothermal contexts, analysis of the LST parameter makes possible the detection of ground surface thermal anomalous areas; these can be likely linked to the Earth's interior dynamic (i.e., endogenous processes) leading to volcanic unrest and eruptions [2,21]. Therefore, TIR Remote Sensing can be helpful in the monitoring of dormant or erupting volcanoes worldwide [1,22–27]. However, the accomplishment of this task is only possible when the analyses are performed with appropriate resolution with respect to the volcanic unrest phase. In the case of early pre-eruptive phases, an adoptable strategy might involve Landsat images and the SCA approach to ensure a good spatial and temporal resolution. Nevertheless, in complex active volcanic scenarios, where several processes of different natures can occur, interfering with one another, a simple analysis of the LST time-series may be insufficient for understanding the shallow thermal state of a volcanic site [27,28].

In this study, we use a workflow (Figure 1) to characterize the shallow thermal state of volcanic and hydrothermal areas by analyzing time series of satellite TIR images using the Independent Component Analysis (ICA) technique. In particular, the first step of the workflow relies on the retrieval of LST time series from Landsat-8 (L8) TIRS nighttime acquisitions, which allow for the study of phenomena in the absence of solar radiation and the related effects; this is performed by considering the Radiative Transfer Equation (RTE) based on the use of a single TIR band. We, therefore, estimate the LST parameter with spatial and temporal resolutions equal to 100 m and 16 days, respectively. Then, the second step of the considered workflow deals with the application of the ICA method to the retrieved LST time series. This allows the separation of the multivariate LST dataset into its independent components (ICs) [29–31], which reflects the relative contribution of the main processes and factors affecting its distribution and thus the main thermal regimes of the area. This method has already been successfully applied to study volcanic and hydrothermal environments using different kinds of datasets [32–38].

We apply the proposed workflow to the Campi Flegrei caldera (CFc) volcanic site, which represents a well-suited case study due to the interaction between magmatic sources, hydrothermal processes, and morpho-climatic factors. In particular, the area of interest (AOI) of our study is a narrow zone of the CFc that includes the most interesting sites of the caldera. We first obtained the 2013–2022 LST time series by processing 90 L8 nighttime images. Subsequently, we applied ICA to identify the main thermal patterns. The results clearly show four components related to the different thermal behavior of the volcanic subregions like the Solfatara crater, the Agnano plain and the Astroni crater. Each component was compared with other available independent datasets to understand their related nature, such as the ground-based temperature acquisitions, the Global Navigation Satellite System (GNSS)-derived vertical deformation rate, the recorded seismicity, and the water table time variations. The obtained results point out how the proposed workflow is suitable for the identification of thermal anomalies with different characteristics in the case of evolving volcanic scenarios such as the CFc.
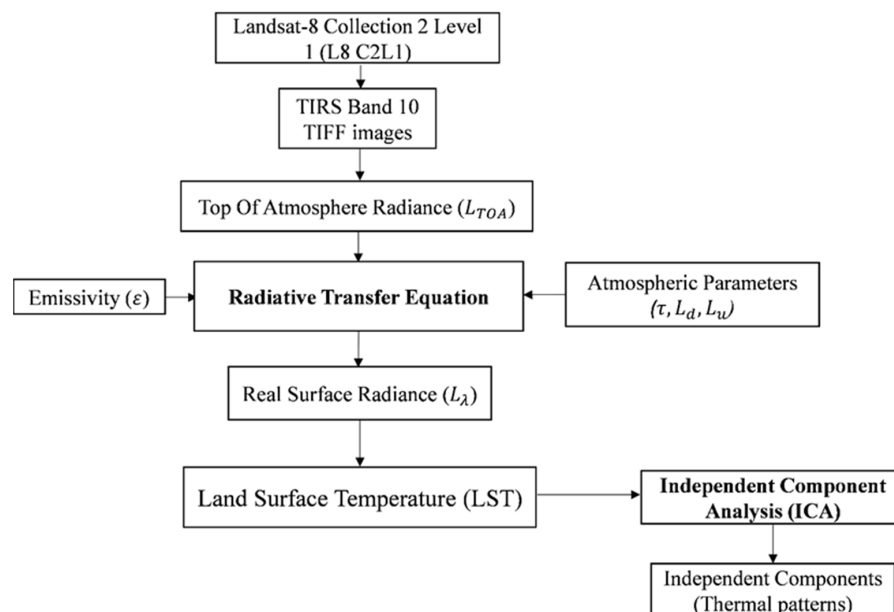
Figure 1. Developed workflow. Operative flowchart used in this work to identify the main thermal patterns of an investigated area.

2. Materials and Methods

In this section, we first describe the Landsat mission and the related products used as input for the proposed analysis. Then, we describe the procedures composing the proposed workflow (Figure 1).

2.1. Landsat Mission

The Landsat mission is a joint mission formulated, implemented, and operated by the National Aeronautics and Space Administration (NASA) and the Department of the Interior U.S. Geological Survey (USGS), which has been collecting imagery of the Earth's surface since 1972 [39]. Landsat products are among the most used to evaluate the LST parameter since the mission provides long-term multispectral acquisition with sufficient spatial and temporal resolutions for this purpose [40]. The latest L8, launched in February 2013, orbits the Earth in a Sun-synchronous, near-polar orbit at an altitude of 705 km with a 16-day repeat coverage, and it is equipped with two sensors: the Operational Land Imager (OLI) and the Thermal Infrared Sensor (TIRS) [41]. The first acquires images in nine spectral bands ranging from the visible (VIS) to the near infrared (NIR), and shortwave infrared (SWIR), with a spatial resolution of 30 m; the second acquires images in two thermal bands centered at 10.9 and 12.0 μm (Band 10 and Band 11, respectively), with a spatial resolution of 100 m [42–45]. Each acquisition is stored in the USGS data catalog [https://earthexplorer.usgs.gov] (accessed on 10 January 2024), where they can be freely downloaded for any area of the world by filtering out the selection using the Worldwide Reference System-2 (WRS-2) path and row parameters. In the framework of the proposed workflow, we consider the nighttime acquisitions related to the TIRS Band 10 (B10) TIFF images and their respective metadata files (MTL). We specify that the cloud cover information is not provided for this kind of product.

2.2. Land Surface Temperature (LST) Retrieval

We use the Radiative Transfer Equation (RTE) to evaluate the LST parameter from L8 TIRS imagery related to a single thermal band (i.e., L8 TIRS B10). We specify that the considered approach requires information about the surface emissivity and the atmospheric components [46,47]. TIRS B10 TIFF images are radiometrically and geometrically corrected, and each pixel of the images is associated with a Digital Number (DN) in an unsigned 16-bit integer format (ranging from 1 to 65,535) [48]. DNs can be converted into Top of

Atmosphere (TOA) radiance values, which represent the radiance arriving at the sensor (L_{TOA}), through the following calibration equation [1,45]:

$$L_{TOA} = M_L \cdot DNs + A_L \tag{1}$$

where:

L_{TOA} is the radiance arriving at the B10 TIRS sensor (W sr^{-1}m^{-2}μm^{-1});
M_L is the multiplicative rescaling factor (=3.342·10^{-4} for L8 B10) from the MTL file;
A_L is the additive rescaling factor (=0.1 for L8 B10) from the MTL file.

However, the atmosphere is not transparent to radiation, so a portion of the radiance emitted by a surface body will always be absorbed and backscattered; this attenuation effect is described by atmospheric transmissivity (τ); also, the atmosphere emits radiation, and the radiance emitted by a surface will be additionally influenced by other atmospheric factors (i.e., the downwelling and upwelling atmospheric radiance components). Thus, the effective radiance arriving at the sensor can be expressed through the RTE as follows [1]:

$$L_{TOA} = \tau \cdot \varepsilon \cdot L_\lambda \cdot L_u + \tau \cdot (1 - \varepsilon) \cdot L_d, \tag{2}$$

where:

L_λ is the real radiance emitted from the surface (W sr^{-1}m^{-2}μm^{-1});
L_u is the upwelling atmospheric radiance component (W sr^{-1}m^{-2}μm^{-1});
L_d is the downwelling atmospheric radiance component (W sr^{-1}m^{-2}μm^{-1});
τ is the atmospheric transmittance (ranging from 0 to 1);
ε is the surface emissivity (ranging from 0 to 1).

After calculating L_{TOA} (Equation (1)), we use the RTE (Equation (2)) to obtain the real radiance of the surface (L_λ). Specifically, here, we estimate the atmospheric parameters (i.e., τ, L_u, and L_d) using MODerate resolution atmospheric TRANsmission (MODTRAN) radiative transfer models [49,50], while the surface emissivity (ε) is extracted from the ASTER Global Emissivity Dataset (ASTER GED version 003), which can be downloaded from the Earth Science Data Systems (ESDS) website [https://search.earthdata.nasa.gov/search] (accessed on 10 January 2024). The scientific datasets contained within the ASTER GED are distributed in HDF5 formats and are composed of five layers; the emissivity layer contains emissivity data for the five TIR bands of ASTER (B10 to B12) with a spatial resolution of 90 m. Finally, we use Plank's equation to retrieve the LST parameter as follows [1,45]:

$$LST = k_2 / [\ln(k_1 / L_{TOA} + 1)], \tag{3}$$

where:

k_1 is the first thermal constant (=774.88853 W sr^{-1}m^{-2}μm^{-1} for L8 B10) provided by the MTL file;
k_2 is the second thermal constant (=1321.0789 K for L8 B10) provided by the MTL file.

2.3. Independent Component Analysis (ICA)

The Independent Component Analysis (ICA) falls within the Blind Source Separation (BSS) techniques [30], which are based on the representation of data in a statistical domain rather than a time or frequency domain. The projection onto another space allows separate data to see hidden important structures [51]. First introduced in the early 1980s [52], ICA, given a mixed signal as input, aims to search for a linear transformation that maximizes the statistical independence between its components, defining in this way the signal's independent components (ICs) [29]. Statistical independence between signal components is assessed by non-Gaussianity, which can be quantified using different properties of random variables, such as kurtosis or negentropy. In comparison with other BSS methods, such as Principal Component Analysis (PCA), the main advantage of ICA is the non-orthogonal component separation that allows for the avoidance of the linear mixing of components. Moreover, with PCA being based on the maximization of signal variance, it produces

uncorrelated but not independent components, which are not equally important like ICs. For these reasons, ICA is more appropriate for the extraction of low-magnitude signals [53].

Within the context of LST retrieval from L8 TIRS imagery, the obtained time series can be represented as $\text{LST}(x_i, t_j)$, where x_i is the position of the ith satellite image pixel, and t_j is the acquisition time of the jth L8 TIRS image. The LST dataset can be decomposed into a finite number of components with fixed spatial patterns. Defining B_k as the spatial pattern of the kth component and A_{jk} as the time-varying amplitudes of the kth component in time t_j, we can write the ICA decomposition as follows [32]:

$$\text{LST}(x_i, t_j) = \sum_{k=1}^{N} A_{jk} \cdot B_k(x_i) \tag{4}$$

In this work, we focus our attention on the spatial patterns (B_k) of the ICs, whose analysis allows for an understanding of the nature of the thermal patterns in the AOI. The finite number of ICs that must be extracted from the input dataset is an a priori information, required for the implementation of ICA. This information can be estimated using different methods [54,55]; here, we use the L-curve method, which is a heuristic approach based on the analysis of the residuals between the input dataset and the decomposed one with a varying number of ICs [56]. Specifically, the L-curve is obtained by plotting these residuals versus the number of the considered components, which may be at most equal to the number of data less one. Finally, the optimal number of ICs is given by the maximal curvature of the L-curve [57].

3. The Case Study of the Campi Flegrei Caldera (CFc)

3.1. Geological and Volcanological Background

The Campi Flegrei caldera (Figure 2) is an active volcanic field in a current state of unrest. The caldera was formed after two major high-energy eruptions: the Campanian Ignimbrite (CI) and the Neapolitan Yellow Tuff (NYT) [58], dated 40 and 15 kyr, respectively [59,60]. Following the eruption of the NYT, the activity of the CFc has generated at least 70 eruptions, which can be subdivided into three epochs of activity [61,62]. Most of the craters can be ascribed to the last epoch (5.5–3.8 kyr), when the Solfatara (4.28 kyr) and Astroni (4.20 kyr) craters were formed [62]. The last eruption of the CFc occurred in 1538 AD, generating the Monte Nuovo composite cone [63,64].
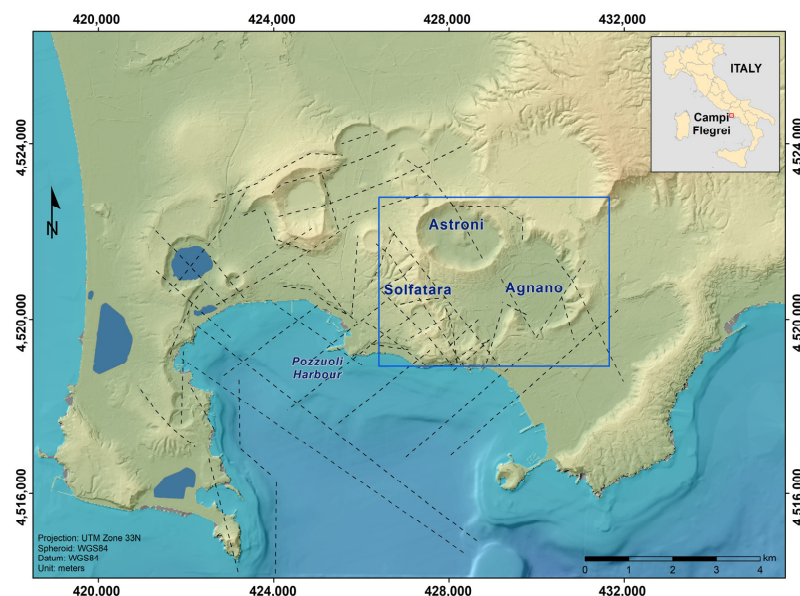

Figure 2. Campi Flegrei caldera. Painted relief map with the main structural features (black dashed lines) of the Campi Flegrei caldera redrawn from [65]. The blue box highlights the Area Of Interest (AOI) of this work. The geographic location map is reported in the upper right corner box.

The CFc is affected by the alternation of subsidence and uplift phases as well as seismicity, also known as bradyseism [66]. The bradyseism episodes are believed to be governed by overpressure of the shallow hydrothermal system, magma movement into the crust, or by both phenomena, e.g., [67–71]. At present, the CFc is experiencing its fourth bradyseism crisis (after the ones in 1945–1953, 1969–1972, and 1982–1984) [72], which started in 2005 with a significant increase in 2012–2013, e.g., [73], when a maximum mean-deformation velocity of about 6 cm/year was recorded at the Pozzuoli harbor [74,75]. The ground vertical movements are also accompanied by frequent seismicity with shallow hypocentral depth (<2 km) [76,77].

The CFc is also characterized by intense hydrothermal activity with the emission of large amounts of deeply derived gases. The most active site is the Solfatara–Pisciarelli area, e.g., [78] where the release of hydrothermal CO_2, through fumarolic vents and soil diffuse degassing, has reached values up to 4000–5000 t/d [79], ranking Campi Flegrei among the top eight volcanic CO_2 emitters on Earth [80] with an estimated energy release of approximately ~100 MW [81]. Another hydrothermally active zone is the Agnano plain, e.g., [82]; the presence of an aquifer at 0 to 3 km beneath this area [83] favors the upward circulation of thermal aquifers [84], which are characterized by high concentrations of CO_2, indicating a contribution of heat and hydrothermal fluids from a magmatic system [85]. These fluids mixing with meteoric waters produce a plume of hot gasses from which steam condenses close to the surface, thus feeding the water table within the Agnano plain [84,86]. Furthermore, the area is characterized by high temperatures with a diffuse surface heat flux reaching 250 mW/m^2 [87].

Together with endogenously active areas, the CFc also includes unique geoenvironmental sites due to the presence of the 30 monogenic edifices inside the caldera. An example is the World Wildlife Fund for Nature (WWF) natural reserve of the Astroni crater [88,89], which is characterized by a microclimate responsible for the distinctive wildlife and the vegetation inversion phenomenon [90].

Furthermore, as one of the most populated active volcanoes on Earth, the CFc is associated with high volcanic risk and is continuously monitored to record any variation in its physical and chemical parameters, which could be interpreted as precursor activity. The Istituto Nazionale di Geofisica e Vulcanologia—Osservatorio Vesuviano (INGV-OV) manages a permanent multi-parametric monitoring network [91]. Regarding thermal monitoring, the CFc is monitored through the ground-based TIR permanent network (TIRNet) [92,93], handheld TIR cameras, and drones [94,95]. Recently, TIR Remote Sensing has become a part of this monitoring network as a supporting tool to detect ground thermal anomalies [27,28,96,97].

3.2. Landsat-8 Data at the CFc

From the USGS data catalog [https://earthexplorer.usgs.gov] (accessed on 10 January 2024), we selected L8 Collection 2 Level 1 (L8 C2L1) scenes of the CFc AOI, which is covered by WRS-2 frame 052/212. We considered the acquisitions during the 2013–2022 time interval and filtered the selection to leave only the nighttime acquisitions (around 20:45 UTC). Furthermore, from a total of 190 nighttime scenes, we manually chose only 90 of them, characterized by low cloud cover, and downloaded the related TIRS B10 TIFF images with their MTL file. The selected dates are not equally distributed over time as reported in Table S1.

According to the proposed workflow, the LST was then evaluated through the RTE algorithm (Equations (2) and (3)) [1]. From ASTER GED version 003, we selected the emissivity information related to ASTER B10, whose resolution was reduced to the same as L8 TIRS B10 (i.e., 100 m). Moreover, for the atmospheric parameters' estimation through MODTRAN, we considered the atmospheric profiles (in terms of altitude, pressure, temperature, and relative humidity) obtained using the Atmospheric Soundings provided by the University of Wyoming [http://weather.uwyo.edu/upperair/sounding.html] (accessed on

10 January 2024) at the nearest meteorological station, which is located at Pratica di Mare, Italy (name: LIRE, number: 16245, latitude: 41.65, and longitude: 12.43).

3.3. LST Time Series at the CFc

Figure 3a shows the LST time series (grey dots) and the related mean temporal trend (blue dots and continuous line) of the AOI during the considered period. We can observe mean LST values ranging from a minimum of 2.5 °C in September 2020, which has been the coolest month of the last few decades, to a maximum of 28.5 °C in June 2022, which has been the hottest month of the hottest year in history since 2003 (for further details, please refer to the Climate Monitoring for Italy report edited by CNR-ISAC and freely available at isac.cnr.it/climstor/DPC/climate_news.html, accessed on 10 January 2024). The mean time series clearly exhibits the oscillating behavior of the temperature due to seasonality. We modeled the seasonal trend through a sinusoidal regression and subtracted the retrieved best-fit pattern (Figure 3b) from the original dataset. The detrended dataset is shown in Figure 3c (grey dots) with mean values (blue dots and continuous line) ranging from a maximum of 20 °C to a minimum of 13.5 °C. The detrended time series also highlights a significant temperature increase of $\approx$1.3 °C/year starting from 2020.
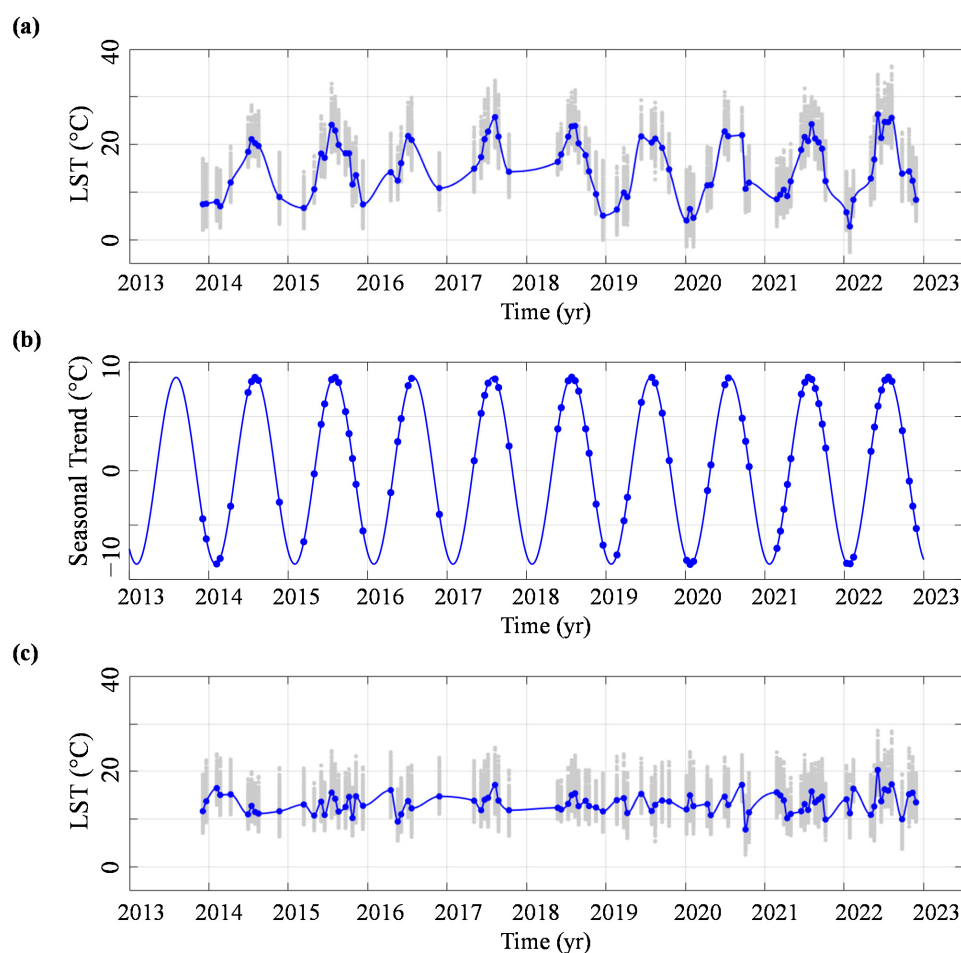

Figure 3. LST time series analysis for the investigated area from 2013 to 2022. Temporal variations of (**a**) the processed LST dataset, (**b**) the retrieved seasonal trend, and (**c**) the detrended LST dataset. Grey dots indicate the temperature values at each pixel of the considered area, while blue dots are the mean values; blue continuous lines express the interpolated trend using mean values.

We then computed the mean maps of the detrended LST for the entire considered period, 2013–2022 (Figure 4), and for each year (Figure S1). In all of the maps, we observed low LST values within the areas of the Astroni crater and the Agnano plain, and higher

LST values near the Solfatara area, where a positive thermal anomaly was identified with a mean LST value > 20 °C.
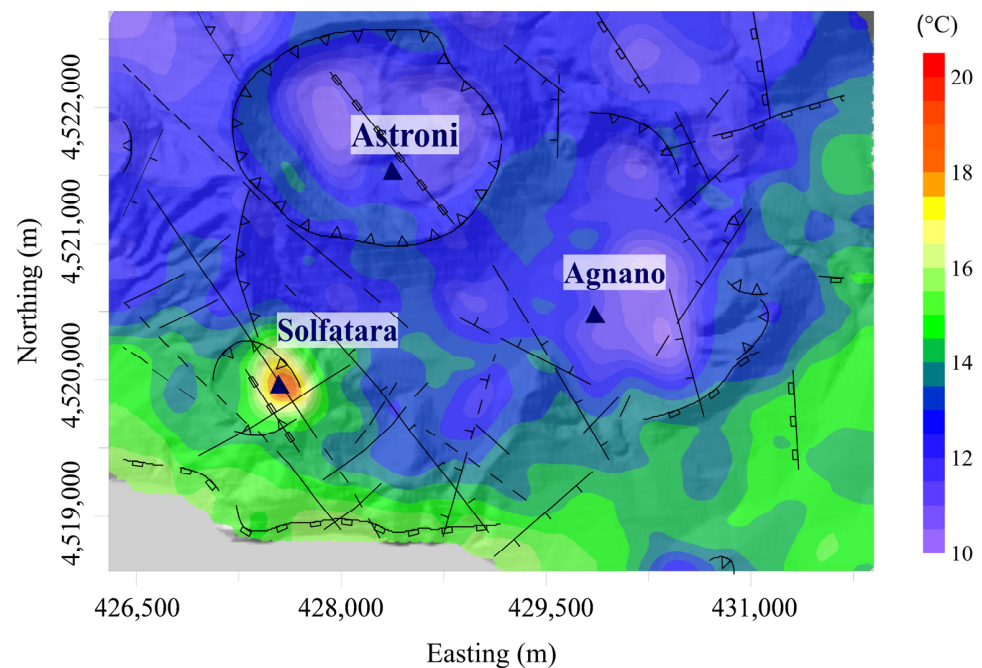

Figure 4. Mean LST map. Detrended mean LST map of the investigated area during the entire considered time period, 2013–2022, superimposed on the structural map redrawn from [65].

3.4. Independent Components of the LST Pattern at the CFc

The application of the L-curve method to our LST dataset allows for the observation of maximum curvature in correspondence with the number of components equal to four (red arrow in Figure 5). We therefore implemented the ICA to the retrieved LST dataset by fixing at four the number of ICs that have to be extracted equally.
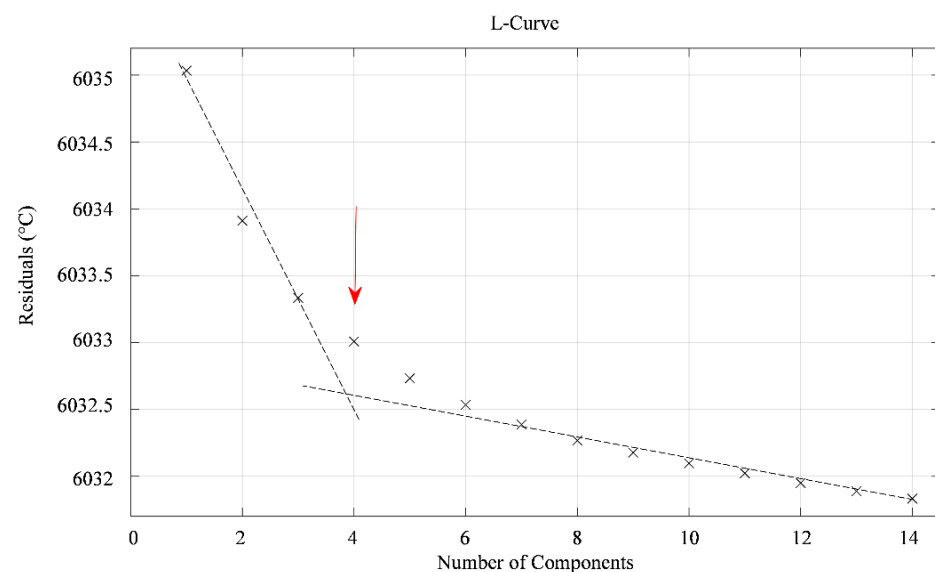
Figure 5. Results of the L-curve method. Analysis of the residuals against the number of components (black crosses); the black dashed lines indicate different slope trends in the L-curve, while the red arrow shows the point where the L-curve has its maximum curvature. The residuals (*y*-axis) are computed as the sum of the squares of the differences between the input dataset and the decomposed one with respect to the number of considered components.

The four extracted ICs are shown in Figure 6 as maps of their spatial patterns normalized with respect to their standard deviation. These maps show the behavior of component subportions in terms of correlation between each other; in particular, areas with the same trend (positive or negative) are correlated, thus sharing the same behavior in terms of LST variations, while areas with opposite trends (different signs of the normalized spatial patterns) are anti-correlated, thus having different behaviors in terms of LST variations.

Figure 6. Independent Component Analysis (ICA) results. Maps of the normalized spatial patterns of the four retrieved ICs superimposed on the AOI structural map redrawn from [65]. The mapped values indicate the correlation among the different subregions of the analyzed area: (**a**) first retrieved IC (IC1); (**b**) second retrieved IC (IC2); (**c**) third retrieved IC (IC3); and (**d**) fourth retrieved IC (IC4).

The performed analysis highlights the following findings: the first component (IC1, Figure 6a) shows an anti-correlation between the Solfatara crater and the remaining CFc sub-portions; the second component (IC2, Figure 6b) highlights an anti-correlation mainly between the Agnano plain and the Solfatara crater; the third component (IC3, Figure 6c) instead identifies an isolated thermal pattern at the Astroni crater, showing no correlation with the surrounding areas; finally, the fourth component (IC4, Figure 6d) does not show a clear correlation pattern with respect to any particular area of the AOI.

4. Discussion

We propose a workflow for the characterization of the surface thermal state and the identification of the main thermal patterns of volcanic areas by analyzing a time series of satellite-derived nighttime LST parameters through ICA. The proposed method therefore allowed for the investigation of thermal anomalous zones, extracting from TIR images the surface temperature rather than other radiative power trends, e.g., [98]. We applied this procedure to study the CFc volcanic area by considering 90 cloud-free nighttime L8 TIRS B10 images during the 2013–2022 time interval.

The first phase of the proposed flowchart (Figure 1) provided the LST time series and maps, which highlighted the presence of one thermal anomaly at the Solfatara crater and surrounding areas with a temporally stable 20 °C value for temperature. We remark that our dataset has a spatial resolution of 100 m, which does not allow for the identification of strictly local phenomena characterized by high temperatures, such as those related to degassing or fumaroles at the Solfatara crater and Pisciarelli fumarole field. Nevertheless, the used dataset enables the identification of this thermal anomalous zone by showing a positive increase of >10 °C when compared with the surroundings. This result confirms the usefulness of satellite-derived temperature data in detecting thermally anomalous zones over large areas.

In the second phase of our workflow, the application of ICA analysis to the retrieved LST dataset allowed for a better investigation of thermal patterns at the CFc. According to the L-curve method, we decomposed our dataset into four components.

IC1 showed a negative correlation between the Solfatara crater and the surrounding areas (Figure 6a). This anti-correlation trend just overlaps with the positive thermal anomaly at the Solfatara crater (Figure 4), which hosts a well-known hydrothermal system with diffuse degassing at La Fangaia, Bocca Nuova, and Bocca Grande sites and where the ground temperature can also exceed 100 °C [99–101]. The Solfatara crater is also characterized by frequent earthquakes [76], and maxima of the deformation field considering the magnitude of the horizontal gradient have been detected [74,75]. We therefore compared IC1 with other available independent information, as follows, in order to understand the nature of the detected anomaly. All of the comparisons were proposed during the 2019–2023 time interval, in which all of the considered datasets were available. The first comparison (Figure 7a) was performed with the ground-based temperature measurements, acquired by the INGV-OV at around 60 ground points located in the Solfatara crater at −0.1 m b.g.l. [https://www.ov.ingv.it/] (accessed on 10 January 2024). The ground temperature trend (red continuous line in Figure 7a) showed higher values with respect to IC1 (blue dots in Figure 7a) and its best-fit polynomial trend (fourth-order: blue continuous line in Figure 7a). This is mainly due to the different resolutions between both of the data; indeed, the ground-based dataset is also able to reflect the effect of the diffuse degassing at the La Fangaia, Bocca Nuova, and Bocca Grande sites. In this context, we remark that satellite-derived measurements are not able to completely frame a strictly local thermal anomaly whose extent is less than their resolving power. Nevertheless, both datasets show comparable stable temporal trends, especially since 2019, when increasing temperatures are recorded in both data. This confirms the reliability of the LST parameter for monitoring purposes.

We performed the second comparison (Figure 7b) considering the local seismicity. Specifically, from the INGV web tool Generator Of Serenade Statistic Pages (GOSSIP) [https://terremoti.ov.ingv.it/gossip/] (accessed on 10 January 2024), we selected the events that occurred beneath the Solfatara crater, with 250 m of maximum horizontal distance from its center, during the 2019–2023 time period, evaluating the seismicity probability density function on a monthly basis (green continuous line in Figure 7b). This shows a positive correlation with respect to IC1 (blue dots in Figure 7b) and its best-fit polynomial trend (fourth-order: blue continuous line in Figure 7b). Specifically, we observed that a clear temperature increase started a few months after the number of earthquakes began increasing (approximately mid-2020 to late-2020). However, the temporal sampling and spatial resolution of the proposed satellite data do not allow us to reliably quantify the possible delay between the two phenomena, and a more complex long-term relationship cannot be satisfactorily argued.

The last comparison is related to the vertical ground deformation derived using the GNSS dataset (Figure 7c). Specifically, we considered the weekly time series recorded at the SOLO station within the Solfatara crater. This station belongs to the continuous Global Positioning System (cGPS) monitoring network of the CFc (for further details on the cGPS network and time series analysis, refer to [102]). We evaluated the monthly vertical deformation rate (orange dots in Figure 7c) and its best-fit polynomial trend (fourth order:

orange continuous line in Figure 7c). The comparison with the analogous IC1 trend (blue dots and continuous line in Figure 7c) shows comparable patterns, with an increase in the deformation rate followed by a temperature increase. Also, in this case, any deeper relationship between the phenomena described by these data cannot be reliably quantified because of the different resolutions of both of the datasets.
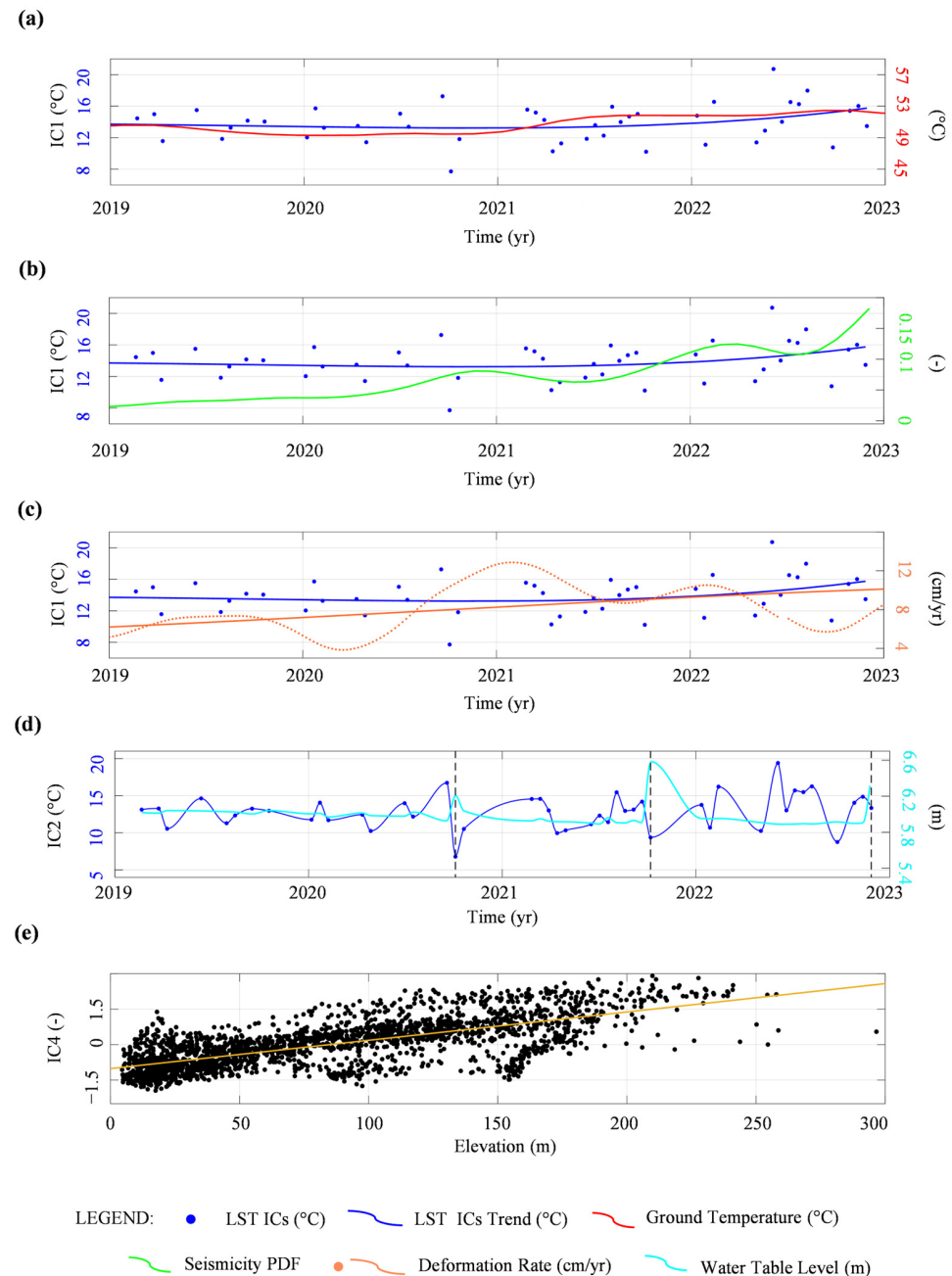

Figure 7. Comparison of the retrieved IC with other datasets. Comparing the retrieved IC1 thermal field (blue dots) and its best-fit fourth-order polynomial trend (blue continuous line) with (**a**) the ground-based temperature trend (red continuous line), (**b**) the seismicity probability density function (green continuous line), (**c**) the cGPS-derived vertical deformation rate (orange dots), and its best-fit fourth-order polynomial trend (orange continuous line). (**d**) Comparison of the interpolated trend (blue continuous line) of the mean IC2 thermal field (blue dots) and the median water table level changes recorded at the Agnano plain (cyan continuous line). (**e**) Correlation plot between the retrieved IC4 spatial pattern and the related altitude; the orange line points out the best-fit linear regression line.

In the end, we associated the thermal anomaly of IC1 with the endogenous processes occurring at the Solfatara hydrothermal system.

IC2 highlighted a correlation pattern for the entire Agnano plain that is in turn anti-correlated with the Solfatara crater. We specify that the Agnano plain is characterized by the circulation of hydrothermal fluids of magmatic origin; these fluids mixing with meteoric waters, in the hydrothermal system, generate a plume of hot gasses from which steam condenses close to the surface, feeding the water table in the area [84,86]. The comparison of IC2 with hydrogeological data has therefore provided more information about this pattern (Figure 7d). We considered the measurements of the water table level variations versus time. This dataset has been collected hourly by the INGV-OV network at a single station in the Agnano plain since 2019. We therefore compared the time series of the mean IC2 LST (blue dots and continuous line in Figure 7d) with the time series of the daily median value of the water table levels (cyan continuous line in Figure 7d), extracted during the period of overlapping between both datasets (i.e., 2019–2023). The comparison clearly showed an anti-correlated behavior (e.g., in October 2021), which is associated with the interaction between the hydrothermal fluids and the meteoric waters. Specifically, during heavy rain episodes, meteoric waters directly feed the water table in the Agnano basin, interacting with the condensed hydrothermal fluids and leading to a rise in the water table level. The presence of water near the surface, due to the different thermal inertia, resulted in a decrease in the LST. In the absence of significant precipitation, the LST values showed that they were not affected by the water table level increase; indeed, positive LST peaks did not correspond to low water table levels.

IC3 identified the isolated thermal pattern of the Astroni crater in functions of no correlation with the surrounding zones. This result may be explained by considering the unique microclimate associated with this area. Actually, because of its concave shape, cold and humid air tends to settle toward the bottom of the crater and is retained because of the absence of air currents due to shielding by the crater slopes; this generates a thermal-inversion phenomenon, which also highly affects the local vegetation, resulting in complementary vegetation-inversion [90]. We therefore interpreted the IC3 thermal pattern as related to microclimatic factors.

The last IC, IC4, did not reveal a particular correlation pattern with respect to the AOI of the CFc. We then investigated the component nature by considering morpho-climatic effects and compared the spatial trend of IC4 with the topography of the area (Figure 7e). Despite the presence of some outliers, the analysis showed a positive correlation between them, with a mean temperature gradient versus altitude of 0.012 °C/m (Figure 7e). This result confirmed the interpretation of the IC4 pattern as related to morphoclimatic factors (e.g., the temperature changes with the altitude and the regime of local winds).

5. Conclusions

In this work, we propose a methodology based on LST retrieval and the application of the ICA technique for the detection of thermal patterns of volcanic zones. This methodology allowed for analysis and understanding of the shallow thermal field of active volcanic and hydrothermal areas and its associations with the different processes occurring, which interact and interfere with each other, at least in terms of the thermal state of the ground surface.

We verified the soundness of the used workflow by analyzing the thermal state of the volcanic site of the CFc. We first constructed the 2013–2022 LST time series and subsequently applied ICA by extracting four thermal patterns with the L-curve method. These are related to the processes occurring at the Solfatara crater, at the Agnano plain, the distinct microclimate of the Astroni crater, and the morphology of the area. The interpretation of the obtained thermal patterns was possible considering other available datasets.

The retrieved results allowed for confirmation of the reliability of satellite data in detecting anomalies of the LST parameter in functions of the related spatial and temporal resolutions and the ability of ICA to extract the thermal components affecting the LST

distribution with different characteristics. The proposed methodology can be defined as a valuable tool to obtain a detailed characterization of the shallow thermal state of any area in the world, especially considering high-risk active volcanic areas, where it can provide support to ground surveillance with the aim of detecting any variation in the thermal field. Furthermore, each extracted component can also be useful for modeling purposes for phenomena of different natures. This study can be followed by future developments related to the integration of thermal images from different satellites (e.g., L8 and ASTER) and drone-based TIR sensors, improving the spatial and temporal resolution of the LST dataset.

Supplementary Materials: The following supporting information can be downloaded at: https://www.mdpi.com/article/10.3390/rs16234615/s1. Table S1: Processed images; Figure S1: Mean LST maps.

Abbreviations

TIR	Thermal InfraRed
LST	Land Surface Temperature
ICA	Independent Component Analysis
ICs	Independent Components
AOI	Area Of Interest
CFc	Campi Flegrei caldera
GOES	Geostationary Environmental Satellites
AVHRR	Advanced Very High-Resolution Radiometer
MODIS	Moderate Resolution Imaging Spectroradiometer
SLSTR	Sea and Land Surface Temperature Radiometer
SCA	Single-Channel Algorithm
MWA	Mono-Window Algorithm
MCA	Multi-Channel algorithm
L8	Landsat-8
RTE	Radiative Transfer Equation
GNSS	Global Navigation Satellite System
NASA	National Aeronautics and Space Administration
USGS	Department of the Interior U.S. Geological Survey
OLI	Operational Land Imager
TIRS	Thermal Infrared Sensor
VIS	Visible
NIR	Near-Infrared
SWIR	Shortwave-Infrared
WRS-2	Worldwide Reference System-2
B10	Band 10

MTL	Metadata file
C2L1	Collection 2 Level 1
DN	Digital Number
TOA	Top of Atmosphere
MODTRAN	MODerate-resolution atmospheric TRANsmission
ASTER GED	ASTER Global Emissivity Dataset
ESDS	Earth Science Data System
BSS	Blind Source Separation
PCA	Principal Component Analysis
CI	Campanian Ignimbrite
NYT	Neapolitan Yellow Tuff
INGV-OV	Istituto Nazionale di Geofisica e Vulcanologia—Osservatorio Vesuviano
GOSSIP	Generator Of Serenade Statistic Pages
cGPS	Continuous Global Positioning System

References

1. Harris, A. Thermal Remote Sensing of Active Volcanoes—A User's Manual. *Bull. Volcanol.* **2014**, *76*, 813. [CrossRef]
2. van der Meer, F.; Hecker, C.; van Ruitenbeek, F.; van der Werff, H.; de Wijkerslooth, C.; Wechsler, C. Geologic Remote Sensing for Geothermal Exploration: A Review. *Int. J. Appl. Earth Obs. Geoinf.* **2014**, *33*, 255–269. [CrossRef]
3. Singh, S. Remote Sensing Applications in Soil Survey and Mapping: A Review. *Int. J. Geomat. Geosci.* **2016**, *7*, 192–203.
4. Khanal, S.; Fulton, J.; Shearer, S. An Overview of Current and Potential Applications of Thermal Remote Sensing in Precision Agriculture. *Comput. Electron. Agric.* **2017**, *139*, 22–32. [CrossRef]
5. Wooster, M.J.; Roberts, G.J.; Giglio, L.; Roy, D.P.; Freeborn, P.H.; Boschetti, L.; Justice, C.; Ichoku, C.; Schroeder, W.; Davies, D.; et al. Satellite Remote Sensing of Active Fires: History and Current Status, Applications and Future Requirements. *Remote Sens. Environ.* **2021**, *267*, 112694. [CrossRef]
6. Norman, J.M.; Becker, B. Terminology in thermal infrared remote sensing of natural surfaces. *Agric. For. Meteorol.* **1995**, *77*, 153–166. [CrossRef]
7. Windahl, E.; Beurs, K.d. An Intercomparison of Landsat Land Surface Temperature Retrieval Methods under Variable Atmospheric Conditions Using in Situ Skin Temperature. *Int. J. Appl. Earth Obs. Geoinf.* **2016**, *51*, 11–27. [CrossRef]
8. Eleftheriou, D.; Kiachidis, K.; Kalmintzis, G.; Kalea, A.; Bantasis, C.; Koumadoraki, P.; Spathara, M.E.; Tsolaki, A.; Tzampazidou, M.I.; Gemitzi, A. Determination of Annual and Seasonal Daytime and Nighttime Trends of MODIS LST over Greece—Climate Change Implications. *Sci. Total Environ.* **2018**, *616–617*, 937–947. [CrossRef]
9. Khan, A.; Chatterjee, S.; Weng, Y. 2—Characterizing Thermal Fields and Evaluating UHI Effects. In *Urban Heat Island Modeling for Tropical Climates*; Khan, A., Chatterjee, S., Weng, Y., Eds.; Elsevier: Amsterdam, The Netherlands, 2021; pp. 37–67. [CrossRef]
10. Brown, C.; Connor, L.N.; Lillibridge, J.; Nalli, N.; Legeckis, R.V. An Introduction to Satellite Sensors, Observations and Techniques. In *Remote Sensing of Coastal Aquatic Environments: Technologies, Techniques and Applications*; Springer: Dordrecht, The Netherlands, 2005; pp. 21–50.
11. Schmetz, J.; Pili, P.; Tjemkes, S.; Just, D.; Kerkmann, J.; Rota, S.; Ratier, A. An introduction to meteosat second generation (MSG). *Bull. Am. Meteorol. Soc.* **2002**, *83*, 977–992. [CrossRef]
12. Sun, D.; Pinker, R.T. Estimation of Land Surface Temperature from a Geostationary Operational Environmental Satellite (GOES-8). *J. Geophys. Res. Atmos.* **2003**, *108*, 4326. [CrossRef]
13. Zhao, W.; Duan, S.-B. Reconstruction of Daytime Land Surface Temperatures under Cloud-Covered Conditions Using Integrated MODIS/Terra Land Products and MSG Geostationary Satellite Data. *Remote Sens. Environ.* **2020**, *247*, 111931. [CrossRef]
14. Li, Z.-L.; Becker, F. Feasibility of Land Surface Temperature and Emissivity Determination from AVHRR Data. *Remote Sens. Environ.* **1993**, *43*, 67–85. [CrossRef]
15. Trigo, I.F.; Ermida, S.L.; Martins, J.P.A.; Gouveia, C.M.; Göttsche, F.-M.; Freitas, S.C. Validation and Consistency Assessment of Land Surface Temperature from Geostationary and Polar Orbit Platforms: SEVIRI/MSG and AVHRR/Metop. *ISPRS J. Photogramm. Remote Sens.* **2021**, *175*, 282–297. [CrossRef]
16. Flynn, L.P.; Harris, A.J.L.; Wright, R. Improved Identification of Volcanic Features Using Landsat 7 ETM+. *Remote Sens. Environ.* **2001**, *78*, 180–193. [CrossRef]
17. Jiménez-Muñoz, J.C.; Sobrino, J.A. A Generalized Single-Channel Method for Retrieving Land Surface Temperature from Remote Sensing Data. *J. Geophys. Res. Atmos.* **2003**, *108*, 4688. [CrossRef]
18. Qin, Z.; Karnieli, A.; Berliner, P. A Mono-Window Algorithm for Retrieving Land Surface Temperature from Landsat TM Data and Its Application to the Israel-Egypt Border Region. *Int. J. Remote Sens.* **2010**, *22*, 3719–3746. [CrossRef]
19. Li, Z.-L.; Tang, B.-H.; Wu, H.; Ren, H.; Yan, G.; Wan, Z.; Trigo, I.F.; Sobrino, J.A. Satellite-Derived Land Surface Temperature: Current Status and Perspectives. *Remote Sens. Environ.* **2013**, *131*, 14–37. [CrossRef]
20. Sekertekin, A.; Bonafoni, S. Land Surface Temperature Retrieval from Landsat 5, 7, and 8 over Rural Areas: Assessment of Different Retrieval Algorithms and Emissivity Models and Toolbox Implementation. *Remote Sens.* **2020**, *12*, 294. [CrossRef]

21. Gemitzi, A.; Dalampakis, P.; Falalakis, G. Detecting Geothermal Anomalies Using Landsat 8 Thermal Infrared Remotely Sensed Data. *Int. J. Appl. Earth Obs. Geoinf.* **2021**, *96*, 102283. [CrossRef]

22. Mia, M.; Nishijima, J.; Fujimitsu, Y. Exploration and Monitoring Geothermal Activity Using Landsat ETM+images. A Case Study at Aso Volcanic Area in Japan. *J. Volcanol. Geotherm. Res.* **2014**, *275*, 14–21. [CrossRef]

23. Eskandari, A.; De Rosa, R.; Amini, S. Remote Sensing of Damavand Volcano (Iran) Using Landsat Imagery: Implications for the Volcano Dynamics. *J. Volcanol. Geotherm. Res.* **2015**, *306*, 41–57. [CrossRef]

24. Blackett, M. Early Analysis of Landsat-8 Thermal Infrared Sensor Imagery of Volcanic Activity. *Remote Sens.* **2014**, *6*, 2282–2295. [CrossRef]

25. Braddock, M.; Biggs, J.; Watson, I.M.; Hutchison, W.; Pyle, D.M.; Mather, T.A. Satellite Observations of Fumarole Activity at Aluto Volcano, Ethiopia: Implications for Geothermal Monitoring and Volcanic Hazard. *J. Volcanol. Geotherm. Res.* **2017**, *341*, 70–83. [CrossRef]

26. Laiolo, M.; Coppola, D.; Barahona, F.; Benítez, J.E.; Cigolini, C.; Escobar, D.; Funes, R.; Gutierrez, E.; Henriquez, B.; Hernandez, A.; et al. Evidences of Volcanic Unrest on High-Temperature Fumaroles by Satellite Thermal Monitoring: The Case of Santa Ana Volcano, El Salvador. *J. Volcanol. Geotherm. Res.* **2017**, *340*, 170–179. [CrossRef]

27. Silvestri, M.; Rabuffi, F.; Pisciotta, A.; Musacchio, M.; Diliberto, I.S.; Spinetti, C.; Lombardo, V.; Colini, L.; Buongiorno, M.F. Analysis of Thermal Anomalies in Volcanic Areas Using Multiscale and Multitemporal Monitoring: Vulcano Island Test Case. *Remote Sens.* **2019**, *11*, 134. [CrossRef]

28. Caputo, T.; Bellucci Sessa, E.; Silvestri, M.; Buongiorno, M.F.; Musacchio, M.; Sansivero, F.; Vilardo, G. Surface Temperature Multiscale Monitoring by Thermal Infrared Satellite and Ground Images at Campi Flegrei Volcanic Area (Italy). *Remote Sens.* **2019**, *11*, 1007. [CrossRef]

29. Comon, P. Independent Component Analysis, A New Concept? *Signal Process.* **1994**, *36*, 287–314. [CrossRef]

30. Cao, X.-R.; Liu, R.-W. General Approach to Blind Source Separation. *IEEE Trans. Signal Process.* **1996**, *44*, 562–571. [CrossRef]

31. Ciaramella, A.; De Lauro, E.; de Martino, S.; Di Lieto, B.; Falanga, M.; Tagliaferri, R. Characterization of Strombolian Events by Using Independent Component Analysis. *Nonlinear Process. Geophys.* **2004**, *11*, 453–461. [CrossRef]

32. Przeor, M.; D'Auria, L.; Pepe, S.; Tizzani, P.; Barone, A.; Vitale, A.; Castaldo, R. Independent Component Analysis and Finite Element Modelling of the 2004-2005 Ground Deformation Unrest in Tenerife (Canary Islands). *Front. Earth Sci.* **2024**, *12*, 1412827. [CrossRef]

33. Ciaramella, A.; De Lauro, E.; Falanga, M.; Petrosino, S. Automatic Detection of Long-Period Events at Campi Flegrei Caldera (Italy). *Geophys. Res. Lett.* **2011**, *38*, L18302. [CrossRef]

34. Cusano, P.; Caputo, T.; De Lauro, E.; Falanga, M.; Petrosino, S.; Sansivero, F.; Vilardo, G. Tracking the Endogenous Dynamics of the Solfatara Volcano (Campi Flegrei, Italy) through the Analysis of Ground Thermal Image Temperatures. *Atmosphere* **2021**, *12*, 940. [CrossRef]

35. Przeor, M.; D'Auria, L.; Pepe, S.; Tizzani, P.; Cabrera-Pérez, I. Elastic Interaction between Mauna Loa and Kīlauea Evidenced by Independent Component Analysis. *Sci. Rep.* **2022**, *12*, 19863. [CrossRef] [PubMed]

36. Barnie, T.; Oppenheimer, C. Extracting High Temperature Event radiance from satellite images and correcting for saturation using Independent Component Analysis. *Remote Sens. Environ.* **2015**, *158*, 56–68. [CrossRef]

37. Bottiglieri, M.; Falanga, M.; Tammaro, U.; Obrizzo, F.; De Martino, P.; Godano, C.; Pingue, F. Independent component analysis as a tool for ground deformation analysis. *Geophys. J. Int.* **2007**, *168*, 1305–1310. [CrossRef]

38. Ebmeier, S.K. Application of independent component analysis to multitemporal InSAR data with volcanic case studies. *J. Geophys. Res. Solid Earth* **2016**, *121*, 8970–8986. [CrossRef]

39. USGS. *Landsat—Earth Observation Satellites*; Fact Sheet 2015-3081; U.S. Geological Survey: Reston, VA, USA, 2015. [CrossRef]

40. Cheng, J.; Meng, X.; Dong, S.; Liang, S. Generating the 30-m Land Surface Temperature Product over Continental China and USA from Landsat 5/7/8 Data. *Sci. Remote Sens.* **2021**, *4*, 100032. [CrossRef]

41. USGS. *Landsat-8 (L8) Data Users Handbook*; Version 5.0; EROS: Sioux Falls, SD, USA, 2019.

42. Thome, K.; Lunsford, A.; Montanaro, M.; Reuter, D.; Smith, R.; Tesfaye, Z.; Wenny, B. Calibration Plan for the Thermal Infrared Sensor on the Landsat Data Continuity Mission. In *Algorithms and Technologies for Multispectral, Hyperspectral, and Ultraspectral Imagery XVII*; SPIE: Bellingham, WA, USA, 2011; Volume 8048, pp. 389–397. [CrossRef]

43. Irons, J.R.; Dwyer, J.L.; Barsi, J.A. The next Landsat Satellite: The Landsat Data Continuity Mission. *Remote Sens. Environ.* **2012**, *122*, 11–21. [CrossRef]

44. Reuter, D.C.; Richardson, C.M.; Pellerano, F.A.; Irons, J.R.; Allen, R.G.; Anderson, M.; Jhabvala, M.D.; Lunsford, A.W.; Montanaro, M.; Smith, R.L.; et al. The Thermal Infrared Sensor (TIRS) on Landsat 8: Design Overview and Pre-Launch Characterization. *Remote. Sens.* **2015**, *7*, 1135–1153. [CrossRef]

45. USGS. *Landsat Collection 2*; Version 1.1; U.S. Geological Survey Fact Sheet 2021–3002, 4 p; USGS: Reston, VA, USA, 2021. [CrossRef]

46. Yu, X.; Guo, X.; Wu, Z. Land Surface Temperature Retrieval from Landsat 8 TIRS—Comparison between Radiative Transfer Equation-Based Method, Split Window Algorithm and Single Channel Method. *Remote Sens.* **2014**, *6*, 9829–9852. [CrossRef]

47. Ali, S.A.; Parvin, F.; Ahmad, A. Retrieval of Land Surface Temperature from Landsat 8 OLI and TIRS: A Comparative Analysis Between Radiative Transfer Equation-Based Method and Split-Window Algorithm. *Remote Sens. Earth Syst. Sci.* **2023**, *6*, 1–21. [CrossRef]

48. USGS. *Landsat-8-9 Operational Land Imager (OLI)—Thermal Infrared Sensor (TIRS) Collection 2 Level 1 (L1) Data Format Control Book (DFCB)*; Version 6.0; EROS: Sioux Falls, SD, USA, 2020.

49. Berk, A.; Bernstein, L.; Robertson, D. *MODTRAN: A Moderate Resolution Model for LOWTRAN*; Spectral Sciences, Inc.: Burlington, MA, USA, 1987; 40p.

50. Adler-Golden, S.M.; Matthew, M.W.; Bernstein, L.S.; Levine, R.Y.; Berk, A.; Richtsmeier, S.C.; Acharya, P.K.; Anderson, G.P.; Felde, J.W.; Gardner, J.A.; et al. *Atmospheric Correction for Shortwave Spectral Imagery Based on MODTRAN4*; Descour, M.R., Shen, S.S., Eds.; SPIE: Denver, CO, USA, 1999; pp. 61–69. [CrossRef]

51. Clifford, G.D. Blind Source Separation: Principal & Independent Component Analysis. *Biomed. Signal Image Process.* **2008**, 1–47.

52. Herault, J.; Ans, B. Réseaux de Neurones a Synapses Modifiables: Décodage de Messages Sensoriels Composites Par Un Apprentissage Non Supervisé et Permanent. *Comptes Rendus Des Séances De L'académie Des Sci. Série III Sci. De La Vie* **1984**, *299*, 525–528.

53. Hyvärinen, A.; Oja, E. Independent Component Analysis: Algorithms and Applications. *Neural Netw.* **2000**, *13*, 411–430. [CrossRef]

54. Rajan, R.; Rayner, P.J.W. Model order selection for the blind separation of Gaussian sources. *IEE Proc. Vis. Image Signal Process.* **1997**, *144*, 217–223.

55. Teschke, G.; Schulz, J. Estimation of the number of independent signals using measures of multivariate dependence. *IEEE Trans. Signal Process.* **2004**, *52*, 1765–1773.

56. Kindermann, S.; Raik, K. A Simplified L-Curve Method as Error Estimator. *Etna* **2020**, *53*, 217–238. [CrossRef]

57. Hansen, P.C. The L-Curve and Its Use in the Numerical Treatment of Inverse Problems. 2005. Available online: https://www.sintef.no/globalassets/project/evitameeting/2005/lcurve.pdf (accessed on 10 January 2024).

58. Orsi, G.; De Vita, S.; di Vito, M. The Restless, Resurgent Campi Flegrei Nested Caldera (Italy): Constraints on Its Evolution and Configuration. *J. Volcanol. Geotherm. Res.* **1996**, *74*, 179–214. [CrossRef]

59. Giaccio, B.; Hajdas, I.; Isaia, R.; Deino, A.; Nomade, S. High-precision 14C and 40Ar/39Ar dating of the Campanian Ignimbrite (Y-5) reconciles the time-scales of climatic-cultural processes at 40 ka. *Sci. Rep.* **2017**, *7*, 45940. [CrossRef]

60. Deino, A.L.; Orsi, G.; de Vita, S.; Piochi, M. The age of the Neapolitan Yellow Tuff caldera-forming eruption (Campi Flegrei caldera–Italy) assessed by 40Ar/39Ar dating method. *J. Volcanol. Geotherm. Res.* **2004**, *133*, 157–170. [CrossRef]

61. Di Vito, M.A.; Isaia, R.; Orsi, G.; Southon, J.; de Vita, S.; D'Antonio, M.; Pappalardo, L.; Piochi, M. Volcanism and Deformation since 12,000 Years at the Campi Flegrei Caldera (Italy). *J. Volcanol. Geotherm. Res.* **1999**, *91*, 221–246. [CrossRef]

62. Smith, V.C.; Isaia, R.; Pearce, N.J.G. Tephrostratigraphy and glass compositions of post-15 kyr Campi Flegrei eruptions: Implications for eruption history and chronostratigraphic markers. *Quat. Sci. Rev.* **2011**, *30*, 3638–3660. [CrossRef]

63. Di Vito, M.; Lirer, L.; Mastrolorenzo, G.; Rolandi, G. The 1538 Monte Nuovo eruption (Campi Flegrei, Italy). *Bull. Volcanol.* **1987**, *49*, 608–615. [CrossRef]

64. Di Vito, M.A.; Acocella, V.; Aiello, G.; Barra, D.; Battaglia, M.; Carandente, A.; Del Gaudio, C.; de Vita, S.; Ricciardi, G.P.; Ricco, C.; et al. Magma Transfer at Campi Flegrei Caldera (Italy) before the 1538 AD Eruption. *Sci. Rep.* **2016**, *6*, 32245. [CrossRef] [PubMed]

65. Bellucci Sessa, E.; Milano, G. Ground uplift and seismic activity at Campi Flegrei caldera (south Italy) during the unrest episodes: An overview. *Bull. Geophys. Oceanogr.* **2024**. [CrossRef]

66. Orsi, G. Volcanic and Deformation History of the Campi Flegrei Volcanic Field, Italy. In *Campi Flegrei: A Restless Caldera in a Densely Populated Area*; Orsi, G., D'Antonio, M., Civetta, L., Eds.; Active Volcanoes of the World; Springer: Berlin/Heidelberg, Germany, 2022; pp. 1–53. [CrossRef]

67. Giudicepietro, F.; Macedonio, G.; Martini, M. A Physical Model of Sill Expansion to Explain the Dynamics of Unrest at Calderas with Application to Campi Flegrei. *Front. Earth Sci.* **2017**, *5*, 54. [CrossRef]

68. Todesco, M. Signals from the Campi Flegrei hydrothermal system: Role of a "magmatic" source of fluids. *J. Geophys. Res. Solid Earth* **2009**, *114*, B05201. [CrossRef]

69. Nespoli, M.; Tramelli, A.; Belardinelli, M.E.; Bonafede, M. The effects of hot and pressurized fluid flow across a brittle layer on the recent seismicity and deformation in the Campi Flegrei caldera (Italy). *J. Volcanol. Geotherm. Res.* **2023**, *443*, 107930. [CrossRef]

70. Giacomuzzi, G.; Chiarabba, C.; Bianco, F.; De Gori, P.; Agostinetti, N.P. Tracking transient changes in the plumbing system at Campi Flegrei Caldera. *Earth Planet. Sci. Lett.* **2024**, *637*, 118744. [CrossRef]

71. Tizzani, P.; Fernàndez, J.; Vitale, A.; Escayo, J.; Barone, A.; Castaldo, R.; Pepe, S.; De Novellis, V.; Solaro, G.; Pepe, A.; et al. 4D imaging of the volcano feeding system beneath the urban area of the Campi Flegrei caldera. *Remote Sens. Environ.* **2024**, *315*, 114480. [CrossRef]

72. Del Gaudio, C.; Aquino, I.; Ricciardi, G.P.; Ricco, C.; Scandone, R. Unrest episodes at Campi Flegrei: A reconstruction of vertical ground movements during 1905–2009. *J. Volcanol. Geotherm. Res.* **2010**, *195*, 48–56. [CrossRef]

73. Di Luccio, F.; Pino, N.A.; Piscini, A.; Ventura, G. Significance of the 1982–2014 Campi Flegrei seismicity: Preexisting structures, hydrothermal processes, and hazard assessment. *Geophys. Res. Lett.* **2015**, *42*, 7498–7506. [CrossRef]

74. Pepe, S.; De Siena, L.; Barone, A.; Castaldo, R.; D'Auria, L.; Manzo, M.; Casu, F.; Fedi, M.; Lanari, R.; Bianco, F.; et al. Volcanic Structures Investigation through SAR and Seismic Interferometric Methods: The 2011–2013 Campi Flegrei Unrest Episode. *Remote Sens. Environ.* **2019**, *234*, 111440. [CrossRef]

75. Castaldo, R.; Tizzani, P.; Solaro, G. Inflating Source Imaging and Stress/Strain Field Analysis at Campi Flegrei Caldera: The 2009–2013 Unrest Episode. *Remote Sens.* **2021**, *13*, 2298. [CrossRef]

76. Tramelli, A.; Giudicepietro, F.; Ricciolino, P.; Chiodini, G. The Seismicity of Campi Flegrei in the Contest of an Evolving Long Term Unrest. *Sci. Rep.* **2022**, *12*, 2900. [CrossRef]

77. Danesi, S.; Pino, N.A.; Carlino, S.; Kilburn, C.R. Evolution in unrest processes at Campi Flegrei caldera as inferred from local seismicity. *Earth Planet. Sci. Lett.* **2024**, *626*, 118530. [CrossRef]

78. Isaia, R.; Vitale, S.; Di Giuseppe, M.G.; Iannuzzi, E.; D'Assisi Tramparulo, F.; Troiano, A. Stratigraphy, structure, and volcano-tectonic evolution of Solfatara maar-diatreme (Campi Flegrei, Italy). *Bulletin* **2015**, *127*, 1485–1504. [CrossRef]

79. Chiodini, G.; Caliro, S.; Avino, R.; Bini, G.; Giudicepietro, F.; De Cesare, W.; Ricciolino, P.; Aiuppa, A.; Cardellini, C.; Petrillo, Z.; et al. Hydrothermal Pressure-Temperature Control on CO_2 Emissions and Seismicity at Campi Flegrei (Italy). *J. Volcanol. Geotherm. Res.* **2021**, *414*, 107245. [CrossRef]

80. Aiuppa, A.; Fischer, T.P.; Plank, T.; Bani, P. CO_2 Flux Emissions from the Earth's Most Actively Degassing Volcanoes, 2005–2015. *Sci. Rep.* **2019**, *9*, 5442. [CrossRef]

81. Chiodini, G.; Frondini, F.; Cardellini, C.; Granieri, D.; Marini, L.; Ventura, G. CO_2 degassing and energy release at Solfatara volcano, Campi Flegrei, Italy. *J. Geophys. Res. Solid Earth* **2001**, *106*, 16213–16221. [CrossRef]

82. Iorio, M.; Punzo, M.; Carotenuto, A.; Cavuoto, C.; Corniello, A.; Di Fiore, V.; Donnaruma, G.; Fedi, M.; Massarotti, N.; Pelosi, N.; et al. Shallow geothermal field multidisciplinary exploration: New data from Campi Flegrei caldera (CFc) for low—Middle enthalpy resource exploration. *Geothermics* **2024**, *121*, 103049. [CrossRef]

83. De Siena, L.; Del Pezzo, E.; Bianco, F. Seismic Attenuation Imaging of Campi Flegrei: Evidence of Gas Reservoirs, Hydrothermal Basins, and Feeding Systems. *J. Geophys. Res. Solid Earth* **2010**, *115*, B09312. [CrossRef]

84. Troiano, A.; Isaia, R.; Di Giuseppe, M.G.; Tramparulo, F.D.A.; Vitale, S. Deep Electrical Resistivity Tomography for a 3D picture of the most active sector of Campi Flegrei caldera. *Sci. Rep.* **2019**, *9*, 15124. [CrossRef]

85. Venturi, S.; Tassi, F.; Bicocchi, G.; Cabassi, J.; Capecchiacci, F.; Capasso, G.; Vaselli, O.; Ricci, A.; Grassa, F. Fractionation Processes Affecting the Stable Carbon Isotope Signature of Thermal Waters from Hydrothermal/Volcanic Systems: The Examples of Campi Flegrei and Vulcano Island (Southern Italy). *J. Volcanol. Geotherm. Res.* **2017**, *345*, 46–57. [CrossRef]

86. Capuano, P.; Russo, G.; Civetta, L.; Orsi, G.; D'Antonio, M.; Moretti, R. The Active Portion of the Campi Flegrei Caldera Structure Imaged by 3-D Inversion of Gravity Data. *Geochem. Geophys. Geosyst.* **2013**, *14*, 4681–4697. [CrossRef]

87. Castaldo, R.; D'Auria, L.; Pepe, S.; Solaro, G.; De Novellis, V.; Tizzani, P. The Impact of Crustal Rheology on Natural Seismicity: Campi Flegrei Caldera Case Study. *Geosci. Front.* **2019**, *10*, 453–466. [CrossRef]

88. Isaia, R.; Di Giuseppe, M.G.; Troiano, A.; Avino, R.; Caliro, S.; Santi, A.; Vitale, S. Structure and present state of the Astroni Volcano in the Campi Flegrei caldera in Italy based on multidisciplinary investigations. *Geochem. Geophys. Geosyst.* **2022**, *23*, e2022GC010534. [CrossRef]

89. Tassi, F.; Randazzo, A.; Venturi, S.; Repetto, A.; Fazi, S.; Amalfitano, S.; Vimercati, L.; Butturini, A.; Caliro, S.; Cuoco, E.; et al. Integrated geochemical and microbiological assessments of Astroni lakes reveals Campi Flegrei unrest signatures. *J. Volcanol. Geotherm. Res.* **2024**, *452*, 108132. [CrossRef]

90. D'Antonio, C. Odonata of the State Nature Reserve "Astroni Crater" near Naples, Southern Italy. *Not. Odonatol.* **1996**, *4*, 116–118.

91. Bianco, F.; Caliro, S.; De Martino, P.; Orazi, M.; Ricco, C.; Vilardo, G.; Aquino, I.; Augusti, V.; Avino, R.; Bagnato, E.; et al. The Permanent Monitoring System of the Campi Flegrei Caldera, Italy. In *Campi Flegrei: A Restless Caldera in a Densely Populated Area*; Orsi, G., D'Antonio, M., Civetta, L., Eds.; Active Volcanoes of the World; Springer: Berlin/Heidelberg, Germany, 2022; pp. 219–237. [CrossRef]

92. Sansivero, F.; Vilardo, G. Twenty Years of Thermal Infrared Observations (2004–2024) at Campi Flegrei Caldera (Italy) by the Permanent Surveillance Ground Network of INGV-Osservatorio Vesuviano. *Remote Sens.* **2024**, *16*, 3352. [CrossRef]

93. Sansivero, F.; Vilardo, G. Processing Thermal Infrared Imagery Time-Series from Volcano Permanent Ground-Based Monitoring Network. Latest Methodological Improvements to Characterize Surface Temperatures Behavior of Thermal Anomaly Areas. *Remote Sens.* **2019**, *11*, 553. [CrossRef]

94. Marotta, E.; Peluso, R.; Avino, R.; Avvisati, G.; Bellucci Sessa, E.; Belviso, P.; Caputo, T.; Carandente, A.; Cirillo, F.; Pescione, R.A. Clusterisation and Temporal Trends of Heat Flux by UAS Thermal Camera. *Remote Sens.* **2024**, *16*, 1102. [CrossRef]

95. Marotta, E.; Peluso, R.; Avino, R.; Belviso, P.; Caliro, S.; Carandente, A.; Chiodini, G.; Macedonio, G.; Avvisati, G.; Marfè, B. Thermal Energy Release Measurement with Thermal Camera: The Case of La Solfatara Volcano (Italy). *Remote Sens.* **2019**, *11*, 167. [CrossRef]

96. Silvestri, M.; Cardellini, C.; Chiodini, G.; Buongiorno, M.F. Satellite-Derived Surface Temperature and in Situ Measurement at Solfatara of Pozzuoli (Naples, Italy). *Geochem. Geophys. Geosyst.* **2016**, *17*, 2095–2109. [CrossRef]

97. Caputo, T.; Bellucci Sessa, E.; Marotta, E.; Caputo, A.; Belviso, P.; Avvisati, G.; Peluso, R.; Carandente, A. Estimation of the Uncertainties Introduced in Thermal Map Mosaic: A Case of Study with PIX4D Mapper Software. *Remote Sens.* **2023**, *15*, 4385. [CrossRef]

98. Aveni, S.; Laiolo, M.; Campus, A.; Massimetti, F.; Coppola, D. TIRVolcH: Thermal Infrared Recognition of Volcanic Hotspots. A single band TIR-based algorithm to detect low-to-high thermal anomalies in volcanic regions. *Remote Sens. Environ.* **2024**, *315*, 114388. [CrossRef]

99. Aucelli, P.P.C.; Brancaccio, L.; Cinque, A. Vesuvius and Campi Flegrei: Volcanic History, Landforms and Impact on Settlements. In *Landscapes and Landforms of Italy*; Soldati, M., Marchetti, M., Eds.; World Geomorphological Landscapes; Springer International Publishing: Cham, Switzerland, 2017; pp. 389–398. [CrossRef]

100. Cardellini, C.; Chiodini, G.; Frondini, F.; Avino, R.; Bagnato, E.; Caliro, S.; Lelli, M.; Rosiello, A. Monitoring Diffuse Volcanic Degassing during Volcanic Unrests: The Case of Campi Flegrei (Italy). *Sci. Rep.* **2017**, *7*, 6757. [CrossRef]

101. Chiodini, G.; Caliro, S.; Avino, R.; Bagnato, E.; Capecchiacci, F.; Carandente, A.; Cardellini, C.; Minopoli, C.; Tamburello, G.; Tripaldi, S.; et al. The Hydrothermal System of the Campi Flegrei Caldera, Italy. In *Campi Flegrei: A Restless Caldera in a Densely Populated Area*; Orsi, G., D'Antonio, M., Civetta, L., Eds.; Springer: Berlin/Heidelberg, Germany, 2022; pp. 239–255. [CrossRef]

102. De Martino, P.; Dolce, M.; Brandi, G.; Scarpato, G.; Tammaro, U. The Ground Deformation History of the Neapolitan Volcanic Area (Campi Flegrei Caldera, Somma–Vesuvius Volcano, and Ischia Island) from 20 Years of Continuous GPS Observations (2000–2019). *Remote Sens.* **2021**, *13*, 2725. [CrossRef]